Journal of Materials Chemistry A

ROYAL SOCIETY OF CHEMISTRY

PAPER

View Article Online
View Journal | View Issue

Cite this: J. Mater. Chem. A, 2025, 13, 12216

Controlled oxidation of V_2O_5/VO_2 hollow nanospheres as photocathodes for photo-rechargeable zinc ion batteries with an ultrahigh capacity enhancement†

Hongran Yang,[a] Shilei Wu,[a] Akesh Manimendra Badalge,[c] Xinyu Li,[c] Qianjin Wang,[ab] Yu Lin Zhong [c] and Ting Zhu *[ab]

Received 19th January 2025
Accepted 17th March 2025

DOI: 10.1039/d5ta00517e

rsc.li/materials-a

Photo-charging batteries are emerging as a new battery technology for large-scale energy storage systems. However, their specific capacity, cycling stability, and light efficiency have reached a bottleneck due to low light-absorption capability, sluggish separation and migration of photoinduced charge carriers, and severe photocorrosion. Herein, hollow nanospheres composed of divanadium pentaoxide/vanadium dioxide (V_2O_5/VO_2) are constructed to broaden light harvesting and improve the redox activity of photo-rechargeable zinc ion batteries (ZIBs). Due to an *in situ* chemical reaction, V_2O_5 and VO_2 are intimately connected to form a V_2O_5/VO_2 heterojunction, thus facilitating the separation and migration of photoinduced charge carriers. As a result, this V_2O_5/VO_2 heterojunction demonstrated a maximum surface photovoltage (SPV) of 25.73 mV, resulting in an ultrahigh specific capacity of 785.6 mA h g^{-1} at 200 mA g^{-1} through a light-discharging process. This delivers a high light enhancement of 77.8% with a power conversion efficiency (PCE) of 4.3%. In addition, ZIBs show promising stability under light irradiation, where a high retention of 53.1% can be achieved even at high current density of 1000 mA g^{-1} after 4000 cycles. This work has pushed forward ZIB technology into a green and sustainable path that can utilize solar energy to promote electrochemical energy storage.

1. Introduction

Solar energy is a green and sustainable energy source that plays an increasing role in energy storage and conversion applications, such as lithium ion batteries (LIBs), zinc ion batteries (ZIBs), supercapacitors (SCs), metal air batteries (MABs), and electrocatalysis (ECs).[1–3] In these energy systems, photo-energy can be harvested using a semiconductor, and the resulting photoinduced charge carriers facilitate charge transfer and accumulation for subsequent storage and conversion. In early 2012, Wang *et al.* demonstrated an integrated power pack composed of a LIB cell and a dye sensitized solar cell (DSSC) employing light-sensitive TiO_2 nanotubes; the LIB cell can be directly charged by the DSSC-based solar cell with an energy conversion and storage efficiency of 0.82%.[4] Subsequent research by Dai *et al.* developed this photo-charging mode by connecting the LIBs to perovskite solar cells, where the photoelectric conversion and storage efficiency was significantly increased to 7.80%.[5] However, the as-reported photo-assisted battery packages contained two separated parts for light-harvesting and charge storage, inevitably leading to a large energy loss and high manufacturing costs.

To alleviate these problems, researchers have proposed the exploration of integrated photo-batteries that can simultaneously harvest light and store charge within a single device.[6] This integration strategy endows a higher potential to provide compact battery devices with lighter weight, further reducing the manufacturing costs, and improving the storage and conversion efficiency.[7] For this optimized type of photo-electric conversion, dual-functional electrode materials should be carefully designed and synthesized to balance the photoelectric properties and electrochemical activity.[8] Typical semiconductive materials such as TiO_2,[9–11] Cu_2O,[12] V_2O_5,[13] Fe_2O_3,[14] and C_3N_4 (ref. 15) with various structures have been employed to serve as dual-functional electrodes for fabrication of the photo-assisted batteries. Recently, Jiang *et al.* described an integrated LIB electrode composed of TiO_2/SnO_2 heterojunctions, where the photogenerated electrons of TiO_2 can be transferred to SnO_2 under light illumination to promote the redox reaction during the charging process. As a result, the specific capacity of the photo-LIBs increased from

[a]School of Physics and Electronic Information, Yunnan Normal University, 768 Juxian Street, Kunming 650500, China. E-mail: zhut0002@ynnu.edu.cn

[b]Yunnan Key Laboratory of Optoelectronic Information Technology, School of Physics and Electronic Information, Yunnan Normal University, Kunming 650500, China

[c]School of Environment and Science, Griffith University, Nathan, QLD 4111, Australia

† Electronic supplementary information (ESI) available: Additional SEM, XRD, UV-vis, electrochemical and calculation data, optical images, *etc.* of the materials and photo-batteries. See DOI: https://doi.org/10.1039/d5ta00517e

1.91 to 3.47 mA h cm^{-2} at 5 mA cm^{-2}, corresponding to a considerable capacity enhancement of 81.6%.[16] Meanwhile, Yang S. Y. *et al.* photoinduced Cu^{+}/Cu^{2+} round-trip valence change in CuO electrode to promote the lithium storage reaction, and the discharge specific capacity can be increased from 539.29 to 580.70 mA h g^{-1} with the assistance of light energy.[17] The increasing reports of introducing light energy into energy storage devices also triggered intensive attention of photo-charging aqueous zinc ion batteries (AZIBs) because AZIBs are considered much cheaper and safer than LIBs while still offering considerable energy density.[18] Pioneering work by Volder *et al.* reported a V_2O_5 nanofiber-based photoactive cathode, by which the gravimetric capacity of the fabricated ZIBs can be elevated from 190 to 370 mA h g^{-1} with photo-conversion efficiencies of ~1.2%.[19] After that, the sample group prepared VO_2 nanorods as dual-functional electrodes for photo-rechargeable AZIBs, and the rate performances can be largely improved with light (photo-conversion efficiency of 0.18% at 455 nm).[20] Despite high capacitance enhancements with improved light efficiencies of photo-batteries (including ZIBs), the detailed mechanisms of photo-assisted enhancement, the separation and migration of photoinduced charge carriers, and capacity decay incurred by photocorrosion are not fully understood. Therefore, it is highly desirable to explore the inter-relationship between the photoelectric property and ZIB performance to understand the charge transfer occurring in the photo-assisted charge–discharge process.

In this work, photocathodes composed of V_2O_5/VO_2 hollow nanospheres are easily constructed to achieve a homogeneous heterojunction that broadens light harvesting and simultaneously enhances redox activity. By compositional and structural design, the surface photovoltage (SPV) of these hollow nanospheres can be optimized to be as high as 30 mV. As a result, the fabricated AZIBs using these V_2O_5/VO_2 hollow nanospheres can deliver a specific capacity of 785.6 mA h g^{-1} at 200 mA g^{-1}, which is much higher than that obtained without light at the same current density (441.8 mA h g^{-1}), corresponding to a light enhancement of 77.8%. In addition, a capacity retention of 53.1% was maintained even at a high current density of 1000 mA g^{-1} for charge–discharge under a full-time test under illumination. Finally, the light power conversion efficiency (PCE) based on a single-wavelength light source (365 nm) was 4.3%. This work demonstrates a designed synthesis of dual-functional V_2O_5/VO_2 photocathodes for AZIBs by tuning the chemical compositions and hollow structures. It exhibits a promising application in the next-generation photo-rechargeable ZIBs.

2. Experimental section

2.1 Synthesis of vanadium-based precursors

In a typical reaction, 5.34 g of oxalic acid ($C_2H_2O_4 \cdot 2H_2O$) was dissolved in 150 mL of deionized (DI) water to form a homogeneous solution. Then, 3 g of commercial V_2O_5 particles was added to the solution to form a yellow suspension under magnetic stirring. The sample was heated in a water bath at 60 °C. Under magnetic stirring, the solution turned from green to blue, which indicated the reduction of V^{5+} to V^{4+} by the formation of vanadium-based precursor. Finally, the product was rinsed with DI water, collected through centrifugation, dried at 75 °C for 2 days, then ground in a mortar to obtain the precursor powder.

2.2 Preparation of VO_2 hollow nanospheres

In a typical procedure, 50 mg of precursor powder was added to a 60 mL solution mixture of methanol and water (4 : 1 vol%). After magnetic stirring for 10 min, the resultant light blue translucent solution was transferred into a 100 mL Teflon-lined stainless-steel autoclave, then heated in an electric air-flow oven at 200 °C for 24 h. After cooling down naturally, the obtained black product was harvested by centrifugation, washed with DI water and ethanol several times before drying overnight at 70 °C.

2.3 Construction of V_2O_5/VO_2 mixed hollow nanospheres

The as-prepared VO_2 nanospheres were annealed at 300 °C for 5 min in a muffle furnace with a heating rate of 2 °C min^{-1} and cooled down naturally before sample collection.

2.4 Material characterization

The morphology and structure were examined by scanning electron microscope (SEM) using a Quanta FEG 250 instrument and transmission electron microscopy (TEM) with high-resolution transmission electron microscopy (HRTEM) with a Tecnai G2 F20 instrument. Thermal gravimetric analysis (TGA) was performed using a thermal tube furnace (Hefei Kejing, GSL-1100X-S-TGA) within a temperature range of 20–300 °C. The chemical states of all the elements in the samples were detected by X-ray photoelectron spectroscopy (XPS) using an ESCALAB250Xi instrument (Thermo Fisher-VG Scientific), and the results were calibrated with a C 1s peak at 284.6 eV. X-ray diffraction was conducted by an X-ray diffractometer (XRD, Rigaku D/max 2500) with Cu Kα radiation (λ = 1.5406 Å) to examine the crystal phases of the samples. Ultraviolet-visible diffuse reflectance spectroscopy (UV-vis DRS) was employed to determine the light adsorption property of the samples using a Shimadzu UV-3600 UV-vis spectrophotometer.

2.5 Preparation of photocathodes

First, the active material, carbon nanotubes, and polyvinylidene fluoride (PVDF 5130) were mixed in a ratio of 7 : 2 : 1 (actual weights of 35 mg, 10 mg, and 5 mg, respectively). Then, 1.5 mL of *N*-methylpyrrolidone (NMP) was added, and the mixture was sonicated for 2 h, with the ultrasonic machine paused every 20 minutes for agitation. After that, 100 μL of the mixture was dropped onto a carbon paper with a loading area of 0.36 π cm^2 (which had been cleaned with alcohol and deionized water, followed by 5 minutes of plasma cleaning). The carbon paper with the loaded material was then transferred to a vacuum oven and dried at 60 °C for 12 h to obtain the final working electrode. The mass loading was approximately 1.8 mg cm^{-2}.

2.6 Fabrication of ZIB full cells

First, an 8 mm round hole was punched in the center of a coin battery (CR2032) shell, and a thin ring of UV adhesive was applied around the edge of the hole. A transparent conductive

ITO was adhered to the punched area to seal the hole window closely using a UV lamp, but allowing light to pass through. A piece of Zn foil anode ($R = 16$ mm, thickness $= 0.05$ mm), V_2O_5/VO_2 photocathode, and glass microfiber separator (Whatman GF/D A6, 16 mm) were assembled in this CR2032-type coin cell with 120 μL of 3 M $Zn(CF_3SO_3)_2$ aqueous electrolyte.

2.7 Electrochemical measurements

All the cyclic voltammetry (CV) cycles, voltage–time (*I–t*) tests, electrochemical impedance spectroscopy (EIS) measurements, rate performances, and long-cycle tests of the ZIBs were conducted using an IVIUM electrochemical workstation (Vertex. C. EIS). Impedance tests were performed within a frequency range of 100 kHz to 0.01 Hz, with a voltage amplitude of 0.01 mV. Galvanostatic charge/discharge (GCCD) curves were obtained using a Neware battery testing system. For the light irradiation measurements of the battery cells, a single-wavelength LED ($\lambda = 365$ nm) was used as the light source. The distance between the light and the battery cell is around 10 cm, and the power of the LED light is ~100 mW cm^{-2}. To ensure long-term electrochemical measurements under illumination, a small fan was placed on one side of the battery to maintain a constant temperature during measurements.

2.8 Theoretical calculation

All computational work was completed in the Cambridge Sequential Total Energy Package (CASTEP), which is a computational software package based on density-functional theory (DFT). The CASTEP can provide atomic-scale descriptions of a wide variety of materials, including studies of surface bonding structures, density of states, optical properties, *etc.* The generalized gradient approximation (GGA) function was used to characterize electron interactions using the Perdew–Burke–Ernzerhof (PBE) approximation and the projector augmented wave (PAW) method was used to characterize electron/ion interactions in atoms. Pure phase VO_2, V_2O_5, and V_2O_5/VO_2 were established, and the space groups of VO_2 and V_2O_5 were *P*2/*C* and *Pmmn*, respectively. The V_2O_5/VO_2 was obtained by cleaving the VO_2 and V_2O_5 along the (001) direction. Additionally, the Monkhorst–Pack K-points for VO_2 and V_2O_5 and V_2O_5/VO_2 were set to $3 \times 3 \times 3$ and $2 \times 2 \times 1$, respectively, and the cutoff energy was 450 eV. In addition, we added a 25 Å vacuum layer to avoid the effect of periodicity in the *z*-axis direction. The valence electron configuration of each atom is [V] $3d^34s^2$ and [O] $2s^22p^6$. For structural optimization, the maximum force convergence accuracy and energy convergence accuracy were taken to be 5×10^{-2} eV $Å^{-1}$ and 1.0×10^{-5} eV per atom, respectively.

3. Results and discussion

The synthetic method for the preparation of V_2O_5/VO_2 hollow nanospheres employed a simple solution/annealing strategy (Fig. 1a). First, vanadium-based precursor (VOC_2O_4) was synthesized by a stirring and drying process using commercial V_2O_5 particles (as shown by the SEM images in Fig. S1†) as

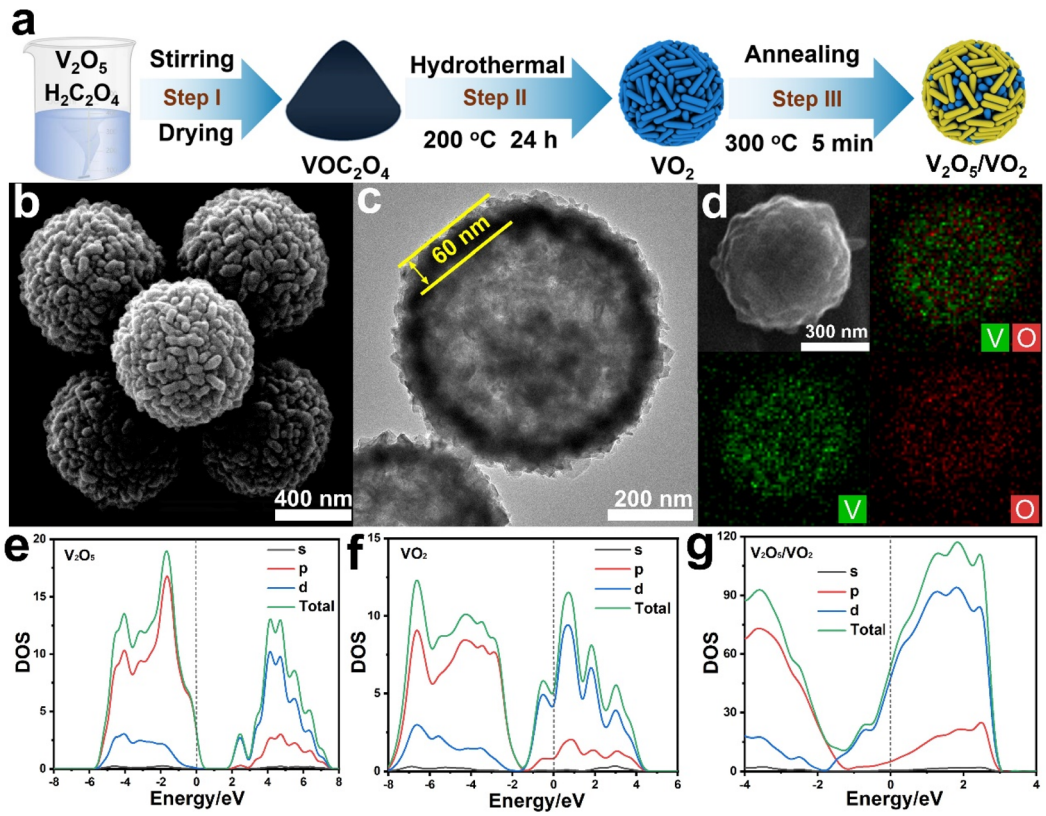

Fig. 1 Synthetic scheme (a), SEM (b), TEM (c) and elemental mapping (d) results of the V_2O_5/VO_2 hollow nanospheres, and density of states of V_2O_5 (e), VO_2 (f), and V_2O_5/VO_2 (g).

a vanadium source (step I). Next, the as-prepared VOC_2O_4 precursor was transformed into VO_2 hollow nanospheres *via* a hydrothermal synthesis with a reaction temperature of 200 °C for 24 h (step II). Finally, the collected VO_2 nanospheres (SEM and XRD shown in Fig. S2 and S3,† respectively) were dried at 60 °C for 12 h and subsequently annealed at 300 °C in air for 5 min to derive the mixed V_2O_5/VO_2 hollow nanospheres (step III).

In our experiments, VO_2 could be completely converted to V_2O_5 if the annealing time was extended to 30 min. Some of the VO_2 of the spheres was *in situ* oxidized to V_2O_5, leading to an intimate contact of these two components. However, the well-defined spheres with the hollow structures can be well maintained after heat treatment, which was confirmed from the SEM image (Fig. 1b). The as-obtained V_2O_5/VO_2 spheres have an average diameter of ~650 nm and are composed of nanosized building units. The structural details with the hollow feature of these nanospheres were further examined by TEM (Fig. 1c). The individual sphere shows a highly porous and hollow texture with a shell thickness of ~60 nm. Elemental mappings were also conducted to examine the elemental distributions of the sphere. V and O are homogeneously interspersed (Fig. 1d), showing the formation of vanadium oxides within the spheres. Theoretical calculations were performed to study the density of states (DOS) of the as-prepared materials. The CASTEP software was used for optimization, and the optimized models are displayed in Fig. S4.† Next, we calculated the band gap of the VO_2 and V_2O_5 pure phases, as well as the V_2O_5/VO_2 heterojunction. The band gap of V_2O_5 is 2.018 eV, while the band gap of VO_2 is 0.165 eV (Fig. S5†). This suggests that V_2O_5 displays a wider bandgap with poor conductivity, whereas VO_2 may exhibit a stronger conductivity. However, the combination of the wide bandgap of V_2O_5 and the metal–insulator transition characteristics of VO_2 results in V_2O_5/VO_2 exhibiting a recombination phenomenon of conduction and valence bands in heterojunction systems that displays metallic characteristics.

The DOS is a significant physical quantity that characterizes the distribution of electronic energy within a material. The DOS of VO_2, V_2O_5, and V_2O_5/VO_2 is illustrated in Fig. 1e–g, with the horizontal axis representing energy. The Fermi level (E_f) is situated at 0 eV, with the valence band positioned to the left and the conduction band to the right of the Fermi level. In Fig. 1e and f, the valence band is predominantly constituted by O 2p orbitals, whereas the conduction band is primarily comprised of V 3d orbitals. Pure phase VO_2 and V_2O_5 exhibit certain electronic states at the Fermi level. However, VO_2 displays a greater number of these states, which results in stronger conductivity properties. Fig. 1g illustrates a substantial concentration of states (free electrons) appearing at the conduction band, which can move freely and improve its electrical properties. In summary, the bandgap and DOS of heterojunctions undergo substantial alterations due to the emergence of interface states. The V_2O_5/VO_2 heterojunction structures exhibit enhanced interface charge transfer performance and broader light absorption capabilities.

To determine the ratio of VO_2 in the V_2O_5/VO_2 spheres, TGA was conducted in a tube furnace with a temperature range from 20 to 300 °C. First, the sample powder was heated from 20 to 300 °C with a heating rate of 2 °C min^{-1} and maintained at 300 °C for 5 min for partial oxidation, followed by another 30 min for complete oxidation (Fig. 2a). As a result, part of the VO_2 was oxidized to V_2O_5 during the annealing by the ratios decreasing, and the ratio of VO_2 in the final V_2O_5/VO_2 sample was determined to be ~20% (annealed at 300 °C for 5 min, indicated by the red dot).

Then, the crystal phases of the as-obtained V_2O_5/VO_2 spheres were examined by XRD (Fig. 2b). All the identified XRD peaks

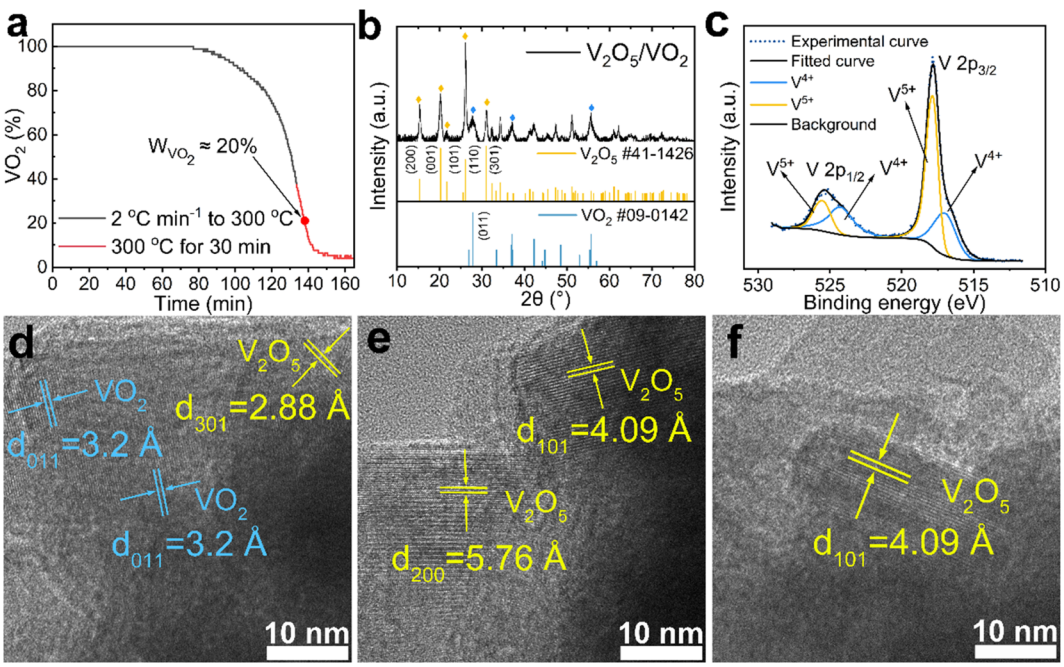

Fig. 2 TGA curve (a), XRD pattern (b), XPS spectra (c), and HR-TEM images (d–f) of the V_2O_5/VO_2 hollow nanospheres.

can be assigned to mixed phases of V_2O_5 (JCPDS 41-1426)[21] and VO_2 (JCPDS 09-0142).[22] In addition, the chemical states of the V elements were determined by XPS (Fig. 2c). The binding energies of 517.6 and 525.5 eV can be assigned to V $2p_{3/2}$ and V $2p_{1/2}$ of V^{5+}, respectively, while the binding energies of 517.2 and 524.7 eV can be attributed to V $2p_{3/2}$ and V $2p_{1/2}$ of V^{4+}, respectively.[23,24] This XPS result confirmed the co-existence of V_2O_5 and VO_2 in the as-constructed nanospheres. To further detect the structural details of the nanospheres, HR-TEM images were obtained to reveal the lattice information of these V_2O_5/VO_2 nanospheres. The inner shell of the hollow sphere reveals the presence of V_2O_5 and VO_2 (Fig. 2d). Specifically, the identified lattice distance of 2.88 Å can be assigned to V_2O_5 (301), while the lattice distances of 3.2 Å is attributed to VO_2 (011). The outer structure of the sphere is more easily oxidized during the annealing process due to better contact with air. Thus, it is reasonable to find that only V_2O_5 is identified in the outer layer of the sphere, which can be confirmed by the presence of (101) and (200) with lattice distances of 4.09 and 5.76 Å, respectively (Fig. 2e). In addition, only V_2O_5 (101) is found at the outmost nanosheets structure, suggesting that the annealing process can facilitate the evolution of V_2O_5 with a specific lattice structure (Fig. 2f). To investigate the light properties of the as-prepared VO_x-based materials, UV-vis analysis was conducted for the V_2O_5, VO_2, and V_2O_5/VO_2 samples between 300–800 nm (Fig. S6†). The intermediate VO_2 sample displayed a narrow light adsorption within 400 nm, corresponding to a calculated bandgap of ~2.95 eV. Meanwhile, the adsorption range of the V_2O_5 sample can be broadened to ~600 nm with a narrower bandgap of 2.06 eV. The bandgap of the material was further narrowed to 1.75 eV with the formation of the V_2O_5/VO_2 heterostructure, which exhibited good light adsorption between 600–800 nm. The as-prepared V_2O_5/VO_2 hollow spheres may present good light harvesting properties for electrochemical Zn^{2+} storage.[25]

Due to the best light adsorption of the V_2O_5/VO_2 sample, Kelvin probe force microscope (KPFM) was employed to further detect the geometry and photoelectric property by a line scanning mode. Fig. 3a and b show the two-dimensional and three-dimensional KPFM images, respectively, of the V_2O_5/VO_2 nanospheres, where the brightness in the images indicates the height of the surface structure. Fig. 3c shows the actual height distribution map of the area indicated by the white line in Fig. 3a. A maximum height of 640 nm was detected, which is very close to the average particle size (650 nm) by the SEM and TEM observations. The surface potentials of the nanospheres with/without light irradiation were measured and compared (Fig. 3d and e), in which higher surface potentials can be obtained with light irradiation compared to those without light. The surface potentials of the selected V_2O_5/VO_2 particles 1–3 by line scanning with/without light irradiation were plotted in Fig. 3f, and the SPV for particles 1–3 were 25.73, 22.07, and 24.59 mV, respectively.

The maximum specific SPV based on the diameter of the nanospheres (~650 nm) was calculated to be ~39.5 kV m^{-1}. A high SPV usually indicates an efficient separation and migration of charge carriers.[26] Before the light charge–discharge measurements, the photocurrent response was evaluated for the as-fabricated ZIB cells (V_2O_5/VO_2/CNTs//Zn, using 3 M $Zn(CF_3SO_3)_2$ aqueous solution as the electrolyte). A steady

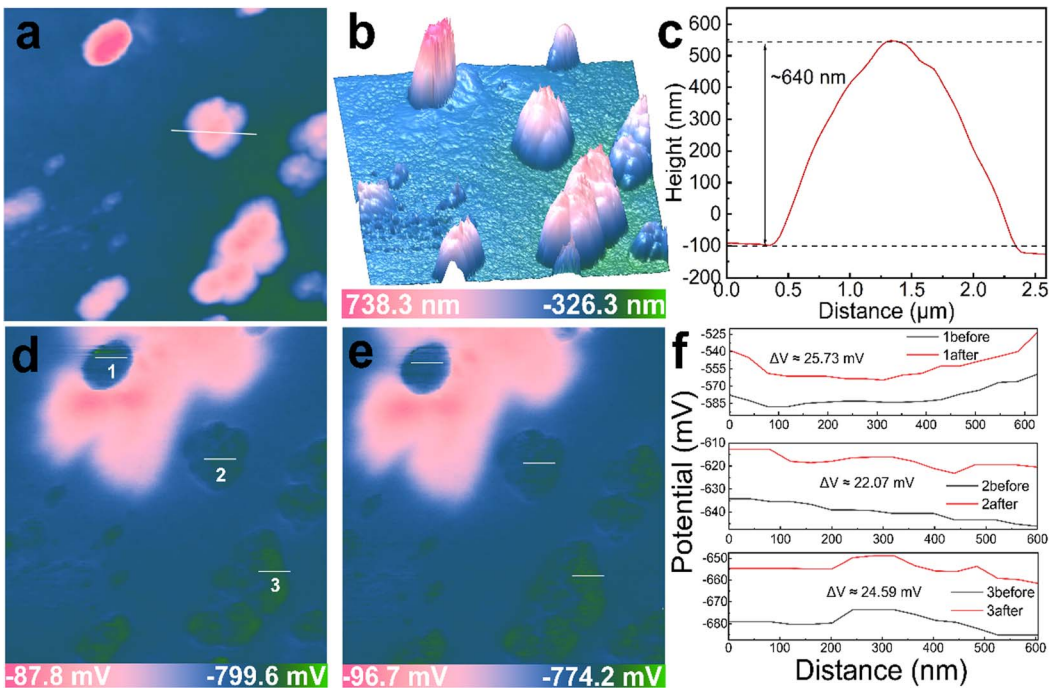

Fig. 3 Two-dimensional (a) and three-dimensional (b) KPFM images, actual height distribution map of the white line section (c), the corresponding KPFM surface potential images without (d) and with (e) light irradiation, and the comparisons of surface potentials with/without light irradiation of the as-prepared V_2O_5/VO_2 nanospheres (f).

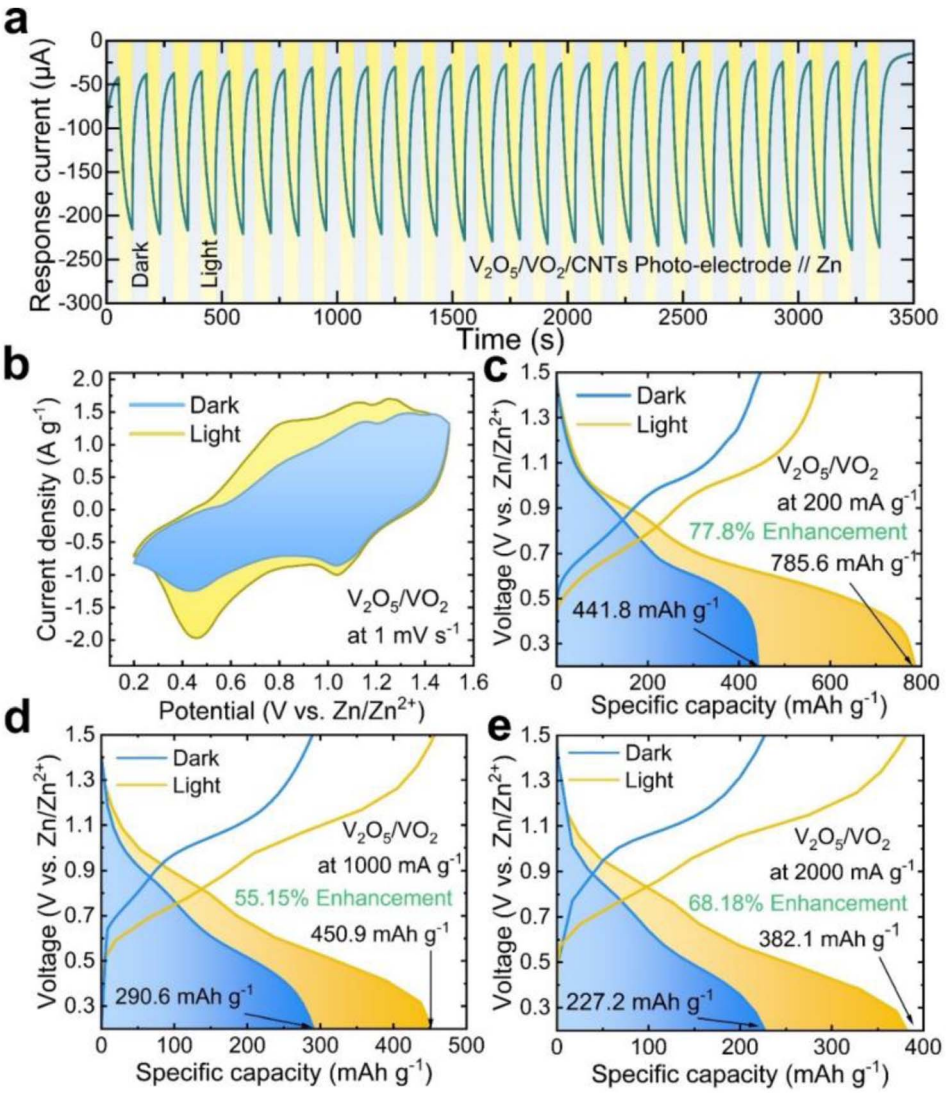

Fig. 4 Photocurrent response (a), CV curves obtained within a potential window of 0.2–1.5 V under dark and light conditions (b), charge–discharge curves obtained at current densities of 200 mA g^{-1} (c), 1000 mA g^{-1} (d), and 2000 mA g^{-1} (e) under dark and light conditions of the as-fabricated ZIBs cells employing V_2O_5/VO_2 as photocathodes.

responsive current is observed under light irradiation (Fig. 4a), with the current value significantly increasing from −48 μA in the dark to ∼220 μA in the light, revealing an enhancement of over 4.5 times. Next, the as-prepared V_2O_5/VO_2 materials were used as photoelectrodes for the fabrication of modified CR2032 coin cells (Fig. S7a and b†), in which a transparent PET film was used to envelop the circular window but allow the light to pass through. Next, CV measurements were conducted for the ZIB cell at a scan rate of 1 mV s^{-1} under dark and light conditions, respectively (Fig. 4b). Two pairs of peaks were observed in the dark (1.14/1.04 V, 0.79/0.45 V), while positively shifted peaks were obtained under light (1.15/1.05 V, 0.8/0.47 V).

Remarkably, a larger CV area can be seen under light conditions compared to that obtained in the dark, revealing the light-enhanced redox reaction occurring in the CV process. Charge–discharge curves performed at various current densities (200–2000 mA g^{-1}) were displayed in Fig. 4c–e, where high enhancements of 55.15–77.8% were calculated under light conditions. The specific discharge capacity at 200 mA g^{-1} was calculated to be 441.8 mA h g^{-1} in the dark and can be increased to 785.6 mA h g^{-1} in the light, delivering the highest enhancement of 77.8%. When the current density was increased to 1000 mA g^{-1}, the specific capacities under dark and light conditions were reduced to 290.6 and 450.9 mA h g^{-1}, respectively. A high specific capacity of 382.1 mA h g^{-1} can be maintained at a current density of 2000 mA g^{-1}, revealing an enhancement of 68.18%. This unusually higher light enhancement at 2000 mA g^{-1} compared with 1000 mA g^{-1} could be caused by the activation of cathode materials under light irradiation. To evaluate the photothermal effect of the materials, the PET film was colored black with a marker pen (Fig. S7c†). At a current density of 1000 mA g^{-1}, the specific discharge capacities obtained in the dark and light were calculated to be 364 and 367 mA h g^{-1}, respectively (Fig. S7d†), which reveals

that the photothermal effect only contributed a capacity enhancement of 0.82%. At 1000 mA g^{-1}, the specific capacities of the intermediate VO_2 cathodes in the dark and light are 437 and 503 mA h g^{-1}, respectively (Fig. S8†), showing a light enhancement of 15.1%. At a higher current density of 2000 mA g^{-1}, the capacity can be enhanced by 18% from 376 to 445 mA h g^{-1}. These results suggest that the V_2O_5 component in the V_2O_5/VO_2 mixed oxide likely enhances the photoelectric conversion due to its superior light absorption capability, thereby additionally contributing to the overall capacity under illumination.[27] The photo-energy enhancement mechanism in this V_2O_5/VO_2-based AZIB is primarily achieved by photo-induced charge transfer and accelerated ion diffusion under illumination, where the light serves as an external driving force that promotes pseudocapacitive surface reactions ($V^{5+} \rightarrow V^{4+}$) and bulk ion diffusion (Zn^{2+}/H^+ intercalation).[28] In addition, the V_2O_5/VO_2 heterostructure forms a built-in electric field at the interface, which reduces the recombination rate of the electrons and holes. This may have enhanced the efficient migration of charged ions, including the intercalation/de-intercalation of Zn ions.

To further evaluate the rate performances of the as-fabricated photo-ZIBs, the discharge specific capacities were obtained at various current densities in the dark and light conditions (Fig. 5a). At a relatively low current density of 200 mA g^{-1}, the capacity increase in the light was calculated as ~27.2% (from 440 to 560 mA h g^{-1}, 40–45th cycles) and can be increased to ~121% (from 230 to 510 mA h g^{-1}) at a higher

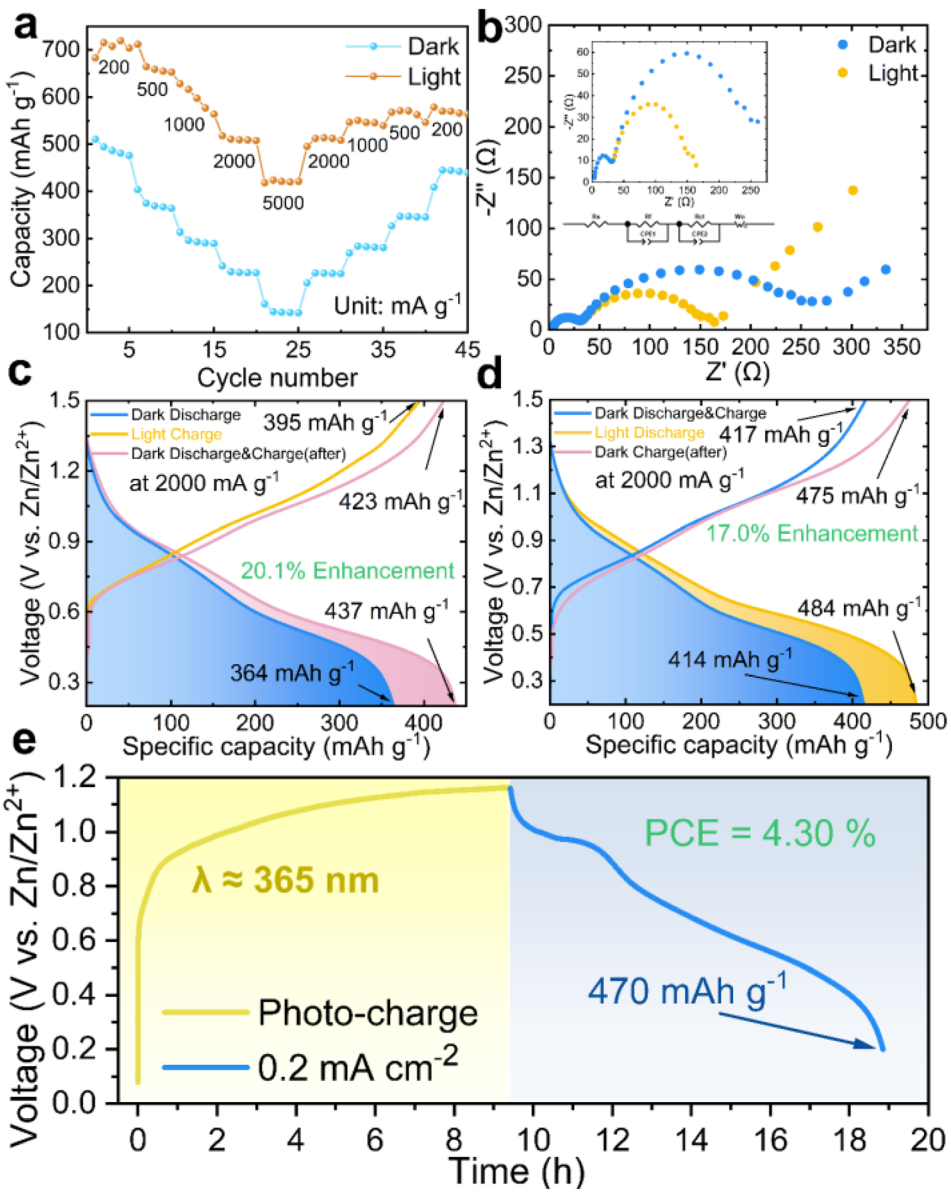

Fig. 5 Rate performances (a), EIS spectra (b), light charge and dark discharge curves obtained at a current density of 2000 mA g^{-1} (c), dark charge and light discharge curves obtained at 2000 mA g^{-1} using a full-spectrum Xe lamp (d), and the light charge and dark discharge curve obtained using a single-wavelength LED light of ~365 nm of the as-fabricated photo-ZIBs (e).

current density of 2000 mA g^{-1}. Illumination can result in a much higher capacity increase of ~180% (from 150 to 420 mA h g^{-1}) at a very high current density of 5000 mA g^{-1}. These rate performances show that the photo-ZIBs prepared herein can deliver better light enhancement at higher current densities, which suggests a great potential for fast-charging of next-generation ZIBs. The EIS plots of the photo-ZIBs clearly show that the contact resistance can be largely reduced upon light irradiation (Fig. 5b). To further investigate the role of light energy in the charge–discharge process, charge/discharge curves under the light and dark conditions were obtained and compared (Fig. 5c). At a current density of 2000 mA g^{-1}, the specific capacity during light charging was calculated as 395 mA h g^{-1} and was maintained at 364 mA h g^{-1} during the dark discharge process. After this round, the photo-battery was re-charged in the dark, and the specific capacity was increased to 423 mA h g^{-1}, which could be caused by the activation of V_2O_5/VO_2 photocathode materials. In addition, the specific capacity obtained by the subsequent dark discharge was calculated as 437 mA h g^{-1}, exhibiting an enhancement of ~20.1% *versus* the first-run discharge capacity. Next, the same battery was recharged in the dark at the same current density and delivered a slightly lower capacity of 417 mA h g^{-1} with a discharge capacity of 414 mA h g^{-1}, respectively (Fig. 5d). After this run, the battery was recharged in the dark again, which has demonstrated a higher capacity of 475 mA h g^{-1}. The re-charged battery was then allowed to discharge in the light, which can deliver a much higher capacity of 484 mA h g^{-1}, corresponding to a light enhancement of ~17%. These results show that light provides additional charge carriers to promote the specific capacities and activates the photocathodes to further improve Zn ion storage.[29] Fig. 5e shows an additional light charge and dark discharge test of the batter at 0.2 mA cm^{-2} to facilitate the calculation of light power efficiency using an LED as the light source (UV-vis spectra, Fig. S6†).

The discharge capacity can be calculated as 470 mA h g^{-1} with a high light PCE of 4.3%. Cycling stability is considered very important to ZIBs and the prolonged cycling tests were conducted for the photo-ZIBs. First, CV measurements of the photo-batteries employing V_2O_5, VO_2, and V_2O_5/VO_2 photocathodes were performed at 1 mV s^{-1} in the light (Fig. 6a), where much higher redox peaks can be observed for the V_2O_5/VO_2-based battery. The V_2O_5/VO_2-based photo-battery was first cycled in the dark at 200 mA g^{-1}, in which the specific capacity increased sharply to ~590 mA h g^{-1}, and then gradually decreased to ~423 mA h g^{-1} after 500 cycles, corresponding to a steady capacity retention of 84.6% (Fig. 6b).

Next, the same battery cell was cycled at a higher current density of 1000 mA g^{-1} in the light to show a potential in fast charge–discharge. The initial discharge capacity was 313.5 mA h g^{-1} and degraded gradually to 166.5 mA h g^{-1} after 4000 cycles, exhibiting a capacity retention of 53.1% and a Coulomb efficiency of ~100% (Fig. 6c). The capacity drop during this long-term cycling test may be partly caused by photo

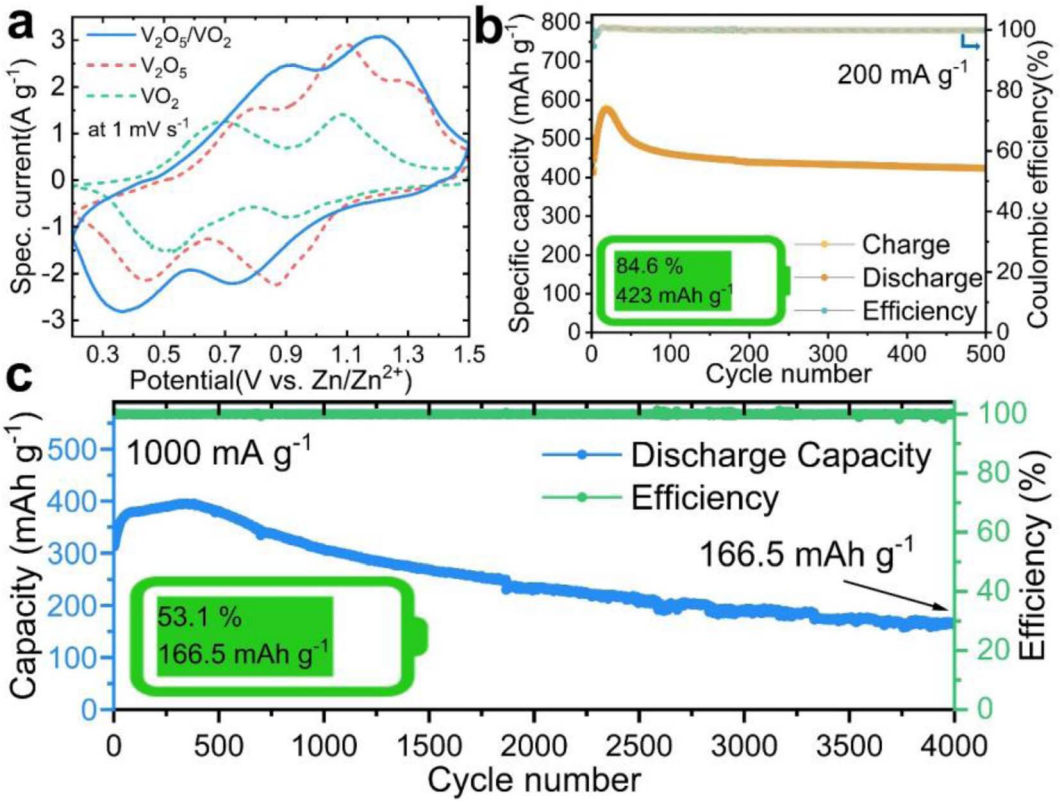

Fig. 6 CV curves of V_2O_5, VO_2, and V_2O_5/VO_2 photocathode-based ZIBs at a scan rate of 1 mV s^{-1} in light (a) and the cycling performances of V_2O_5/VO_2 photocathode-based ZIBs conducted at current densities of 200 mA g^{-1} (b) and 1000 mA g^{-1} (c) of the V_2O_5/VO_2 photocathode-based ZIBs in the light condition.

corrosion of the cathode materials,[30] because the light was applied throughout the cycling tests. In addition, the loss of Zn anode is another important reason for the capacity decay. Thus, the morphology and composition of the cathode after cycling tests were analyzed. After cycling for 500 times at a current density of 5 A g^{-1}, the battery cell was disassembled to collect the cathode material for SEM and EDX characterization (Fig. S9†). Zn particles can be found on the surface of the cathode, suggesting the formation of "dead zinc", which could be another explanation for the capacity decay upon cycling. The F and S elements in mapping are originated from the $Zn(CF_3SO_3)_2$ electrolyte. Consequently, electrolyte additives such as nanocellulose can be used to suppress the Zn dendrites to enhance the long-term performance, and further reduce the photocorrosion of V_2O_5/VO_2 by surface coating of a thin carbon layer. However, the formation of the V_2O_5/VO_2 heterojunction herein could be favorable to enhance the charge separation and migration, thus reducing hole accumulation at the electrode surface.[31] This can minimize the oxidation of VO_2, possibly mitigating the long-term photocorrosion. Finally, The ZIB performances of this work are comparable with those of photo-batteries (including ZIBs and LIBs) reported previously (Table S1, ESI†). To study the crystal and chemical states changes of V_2O_5/VO_2 electrodes during the repeated intercalation and de-intercalation of zinc ions, *ex situ* XRD and XPS analysis were performed for the cathodes (loaded onto carbon cloth, CC) at different charge–discharge states of the ZIB cells. First, XRD patterns of the pristine CC and V_2O_5/VO_2 loaded CC (Fig. S10a†) showed no impurities, with only peaks of V_2O_5 and CC. Next, the V_2O_5/VO_2 loaded CC was cycled and discharged to 1 V and 0.2 V at the 10^{th} cycle (10D1.0 and 10D0.2, Fig. S10b†), respectively. XRD peaks for ZnV_3O_8 can be clearly distinguished, revealing the partial occupation of V sites by Zn. Subsequently, the cells were re-charged to 1 V and 1.5 V again, where XRD peaks for V_3O_7 and $VO(OH)_2$ were detected for the cathodes, showing good reversible properties for Zn intercalation and de-intercalation. In addition, further XPS results show that the intensity for V^{5+} was remarkably reduced when V_2O_5/VO_2 loaded CC was charged to 1.5 V and then discharged to 0.2 V (Fig. S10c†). The intensity for Zn was distinctly increased during this charge–discharge process but without any peak shift of binding energies (Fig. S10d†), verifying the intercalation and de-intercalation of Zn within the V_2O_5/VO_2 cathodes. To evaluate the structural stability of the cathode materials, SEM/EDX and XRD data of the materials were obtained and displayed after 4000 cycles (Fig. S11†). Compared to the dark condition, more $VO(OH)_2$ was formed within the cathode under light conditions (Fig. S11a†), revealing an increased intercalation of hydrated Zn ions under light irradiation. In addition, nanosheet-like layered structures were found (Fig. S11b–d†), which could be due to the formation of hydroxylated species, such as $VO(OH)_2$.

4. Conclusions

Hollow nanospheres composed of V_2O_5/VO_2 mixed oxides were prepared to broaden light harvesting and improve the redox activity of the photocathodes for photo-rechargeable ZIBs. The hollow feature of the spheres was verified by SEM and TEM characterization, while the light sensitivity was confirmed by UV-vis spectra. The highlight of the as-prepared V_2O_5/VO_2 nanospheres is the considerable SPV value, which was examined and confirmed by the KPFM images collected under illuminated and dark conditions. As a result, the photo-batteries employing these V_2O_5/VO_2 hollow nanospheres can realize a maximum specific capacity of 785.6 mA h g^{-1} at a current density of 200 mA g^{-1} in the light, delivering a capacity enhancement of 77.8% with a light PCE of 4.3%. Finally, the photo-battery can present a high cyclic retention of 53.1% even at a high current density of 1000 mA g^{-1} after 4000 cycles during the light charge–discharge process, which indicates a high potential for next-generation photo-rechargeable zinc ion batteries. Importantly, the as-described photo-assisted charging feature may bring great changes in the battery technology by expanding the application scenarios. For example, the portable electronic devices can be automatically charged outdoors or in a solar environment, reducing reliance on traditional chargers.

Data availability

The data supporting this article have been included as part of the ESI.†

Author contributions

H. R. Yang carried out the experiments, collected, and analyzed the data; S. L. Wu and Q. J. Wang assisted the data collection and analysis; T. Zhu conceived the research idea, supervised the project, analyzed the data and wrote the manuscript; A. M. Badalge revised the manuscript. X. Y. Li and Y. L. Zhong provided important discussions and revised the manuscript.

Conflicts of interest

The authors declare no conflict of interest.

Acknowledgements

This work was financially supported by the National Natural Science Foundation of China (grant no. 52263028), and Yunnan Fundamental Research Projects (grant no. 202301AT070059).

References

1 Y.-X. Tan, X. Zhang, J. Lin and Y. Wang, *Energy Environ. Sci.*, 2023, **16**, 2432–2447.
2 M. R. Yang, D. H. Wang, Y. H. Ling, X. N. Guo and W. H. Chen, *Adv. Funct. Mater.*, 2024, 2410398.
3 H. M. Liu, X. R. Gao, Y. T. Lou, H. K. Liu, S. X. Dou, Z. C. Bai and N. N. Wang, *Adv. Energy Mater.*, 2024, 2402381.
4 W. Guo, X. Xue, S. Wang, C. Lin and Z. L. Wang, *Nano Lett.*, 2012, **12**, 2520–2523.
5 J. Xu, Y. Chen and L. Dai, *Nat. Commun.*, 2015, **6**, 8103.
6 A. Paolella, C. Faure, G. Bertoni, S. Marras, A. Guerfi, A. Darwiche, P. Hovington, B. Commarieu, Z. Wang,

M. Prato, M. Colombo, S. Monaco, W. Zhu, Z. Feng, A. Vijh, C. George, G. P. Demopoulos, M. Armand and K. Zaghib, *Nat. Commun.*, 2017, **8**, 14643.
7 J. Lv, J. Xie, A. G. A. Mohamed, X. Zhang and Y. Wang, *Chem. Soc. Rev.*, 2022, **51**, 1511–1528.
8 A. Gouder, F. Podjaski, A. Jiménez-Solano, J. Kröger, Y. Wang and B. V. Lotsch, *Energy Environ. Sci.*, 2023, **16**, 1520–1530.
9 J. H. Li, Y. Q. Zhang, Y. Y. Mao, Y. Y. Zhao, D. X. Kan, K. Zhu, S. L. Chou, X. T. Zhang, C. L. Zhu, J. Ren and Y. J. Chen, *Angew. Chem., Int. Ed.*, 2023, **62**, e202303056.
10 W. Yan, J. Wang, Q. Hu, J. J. Fu, M. K. Albolkany, T. Zhang, X. Lu, F. Ye and B. Liu, *Nano Res.*, 2024, **17**, 2655–2662.
11 S. Yi, Z. Su, H. L. Chen, Z. Q. Zhao, X. W. Wang, Y. Y. Zhang, B. Niu and D. H. Long, *Appl. Catal., B*, 2024, **348**, 123853.
12 T. Zhu, J. Pan, Z. An, R. Zhe, Q. Ou and H.-E. Wang, *J. Mater. Chem. A*, 2022, **10**, 20375–20385.
13 S. Naskar, D. Maity, A. Dixit, M. Freitag, K. Kumari, S. K. Singh and M. Deepa, *J. Mater. Chem. A*, 2024, **12**, 15203–15226.
14 T. Zhu, C. Xia, B. Wu, J. Pan, H. Yang, W. Zhang and B. Y. Xia, *Appl. Catal., B*, 2024, **357**, 124315.
15 R. Ren, G. Liu, J. Y. Kim, R. E. A. Ardhi, M. X. Tran, W. Yang and J. K. Lee, *Appl. Catal., B*, 2022, **306**, 121096.
16 C. Hu, L. Chen, Y. Hu, A. Chen, L. Chen, H. Jiang and C. Li, *Adv. Mater.*, 2021, **33**, 2103558.
17 Q. M. Zhang, M. Wei, Q. W. Dong, Q. Z. Gao, X. Cai, S. S. Zhang, T. Yuan, F. Peng, Y. P. Fang and S. Y. Yang, *J. Energy Chem.*, 2023, **79**, 83–91.
18 H. T. Xu, W. Y. Yang, M. Li, H. B. Liu, S. Q. Gong, F. Zhao, C. L. Li, J. J. Qi, H. H. Wang, W. C. Peng and J. P. Liu, *Small*, 2024, **20**, 2310972.
19 B. D. Boruah, A. Mathieson, B. Wen, S. Feldmann, W. M. Dose and M. De Volder, *Energy Environ. Sci.*, 2020, **13**, 2414–2421.
20 B. Deka Boruah, A. Mathieson, S. K. Park, X. Zhang, B. Wen, L. Tan, A. Boies and M. De Volder, *Adv. Energy Mater.*, 2021, **11**, 2100115.
21 Y. Liu, Y. Liu, X. Wu and Y. R. Cho, *ACS Sustain. Chem. Eng.*, 2023, **11**, 13298–13305.
22 Ü. Ö. A. Arier and B. Ö. Uysal, *Surf. Coat. Technol.*, 2016, **302**, 482–486.
23 S. Zafar, M. Sharma, K. M. P. Shai, N. Karmodak, S. K. Singh and B. Lochab, *J. Mater. Chem. A*, 2024, **12**, 32947–32956.
24 L. Zhang, Y. Xuan, Q. Wang, Z. Zhu, D. Zhao, X. Liu, Q. Zhu and K. Zhang, *J. Mater. Chem. A*, 2024, **12**, 15361–15372.
25 M. Zhang, L. Pan, Z. Jin, X. Wang, H. Mei, L. Cheng and L. Zhang, *Adv. Energy Mater.*, 2023, **13**, 2204058.
26 R. T. Chen, Z. F. Ren, Y. Liang, G. H. Zhang, T. Dittrich, R. Z. Liu, Y. Liu, Y. Zhao, S. Pang, H. Y. An, C. W. Ni, P. W. Zhou, K. L. Han, F. T. Fan and C. Li, *Nature*, 2022, **610**, 296–301.
27 Y. Lu, H. Andersen, R. Wu, A. M. Ganose, B. Wen, A. Pujari, T. Wang, J. Borowiec, I. P. Parkin, M. De Volder and B. D. Boruah, *Small*, 2024, **20**, 2308869.
28 W. W. Zha, Q. S. Ruan, L. Ma, M. Liu, H. W. Lin, L. T. Sun, Z. M. Sun and L. Tao, *Angew. Chem., Int. Ed.*, 2024, **63**, e202400621.
29 M. Wilhelm, R. Adam, A. Bhardwaj, I. Neumann, S. H. Cho, Y. Yamada, T. Sekino, J. Tao, Z. Hong, T. Fischer and S. Mathur, *Adv. Eng. Mater.*, 2023, **25**, 2200765.
30 X. Y. Wen, Y. T. Zhong, S. Chen, Z. C. Yang, P. Y. Dong, Y. Q. Wang, L. H. Zhang, Z. Wang, Y. Jiang, G. F. Zhou, J. M. Liu and J. W. Gao, *Adv. Sci.*, 2024, **11**, 2309555.
31 J. W. Li, Z. Y. Huang, C. Wang, L. Tian, X. Q. Yang, R. F. Zhou, M. N. Ghazzal and Z. Q. Liu, *Appl. Catal., B*, 2024, **340**, 123181.